



Nonisothermal Modeling of Polymer Electrolyte Fuel Cells

II. Parametric Study of Low-Humidity Operation

Hyunchul Ju,^a Chao-Yang Wang,^{a,*} Simon Cleghorn,^b and Uwe Beuscher^{b,**}

^aElectrochemical Engine Center, and Department of Mechanical and Nuclear Engineering, The Pennsylvania State University, University Park, Pennsylvania 16802, USA

^bGore Fuel Cell Technologies, W.L. Gore & Associates, Inc., Elkton, Maryland 21921, USA

A parametric study is carried out using the nonisothermal polymer electrolyte fuel cell (PEFC) model presented in Part I, which was experimentally validated against the current distribution data. The focus is placed on exploring the characteristics of low-humidity operation, including the effects of gas diffusion media tortuosity and thermal conductivity and membrane electrode assembly properties, such as ionomer fraction of the catalyst layer, the cathode kinetic parameter, and the membrane thickness. In addition, the effect of contact resistance is studied and co- and counterflow configurations between the anode and cathode streams are contrasted. The present work elucidates detailed effects of these important design and operating parameters on the current density distribution and assists in identifying optimal water and thermal management strategies for the low-humidity operation of PEFCs.

© 2005 The Electrochemical Society. [DOI: 10.1149/1.2137655] All rights reserved.

Manuscript submitted April 1, 2005; revised manuscript received September 7, 2005. Available electronically December 23, 2005.

The polymer electrolyte fuel cell (PEFC) is considered the most promising technology capable of displacing the internal combustion engine as the power plant for automotive drivetrains. In this application, it is very advantageous to operate the PEFC under low-humidity reactant inlet conditions in order to simplify the fuel cell system, minimizing the system volume and parasitic power required for external humidification and condensation of reagent gases. In this mode of operation, the interactions between water and heat management are especially important, and the calculation of membrane hydration and the resulting proton conductivity becomes a central task in PEFC computer simulations, which requires an accurate and detailed membrane electrode assembly (MEA) model.

Many numerical models have been developed to simulate the effects of various design and operating parameters in PEFCs. Among isothermal models, much effort was focused on investigating the effects of operating temperature, pressure, humidification of gas streams, fuel/air stoichiometry, etc.¹⁻⁴ Additionally, gas diffusion media (GDM) thermal conductivity and thermal boundary conditions, including heat exchanger designs, were also recognized as important factors in nonisothermal PEFC simulations.⁵⁻¹¹ However, most of the prior models are one-dimensional (1D) and, thus, are incapable of capturing multidimensional effects in PEFCs, particularly the inherent multidimensional characteristics of coupled water and heat transport. The few existing parametric studies using 2D or 3D models were also limited to the overall cell performance and not focused on the detailed internal phenomena, such as the current density and membrane water content distributions.

The present work provides an extensive parametric study of low-humidity PEFCs using the fully three-dimensional, electrochemical reaction-transport-thermal coupled PEFC model presented in Part I.¹² We aim to portray the main impact of material properties to develop a basic understanding of low-humidity PEFCs.

Numerical Model

The numerical model and computational geometry have been described in detail in Part I,¹² and thus only a brief summary of the model assumptions is repeated here as follows: (i) ideal gas mixtures; (ii) incompressible and laminar flow due to small pressure gradients and flow velocities; (iii) negligible ohmic potential drop in the electronically conductive solid matrix of porous diffusion and catalyst layers, as well as in the current collectors due to their relatively very large electrical conductivities; and (iv) single-phase flow for water transport (i.e., no liquid water).

Assumption (iv) is valid under the condition that the liquid satu-

ration within the GDL is low or liquid droplets are small and disperse in gas flow to form a mist flow. Therefore, the single-phase approach is particularly well suited for fuel cell simulations under low-humidity operation such as $RH_a/RH_c = 75\%/0\%$ here. Because of assumption (iv), the heat release/absorption due to phase change is also excluded. The present numerical study is focused on investigating the effects of GDM and MEA properties on the current density distribution as well as the overall cell performance. The cell temperature is 80°C with inlet humidity conditions of 75% at the anode and zero at the cathode. Consistent with Part I, the inlet pressure on both anode and cathode is 3.18 atm, and the anode and cathode stoichiometric ratios are set at 1.2 and 2.0, respectively. In addition, the thermal boundary condition is assumed such that all external temperatures of end plates are at 80°C. All calculations were performed at a cell potential of 0.7 V. The simulations were carried out on a ten-node PC cluster (1.4 GHz).

Results and Discussion

Table I summarizes all parametric cases of this study, in which eight parameters are varied between low and high values around their baseline values. In addition, a single counterflow configuration case is compared with the coflow baseline case. In the following discussion, the parametric cases listed in Table I are discussed separately. A parametric case is labeled as "L" for the lower value and "H" for the higher value, preceded by the case number indicated in Table I; for example, the case with the lower value in the macro-GDM tortuosity is denoted by case 1L.

In Cases 1 through 3, the tortuosity effects in the catalyst layer, micro-GDM and macro-GDM, respectively, are investigated. The tortuosity of the GDM influences the effective diffusivity of reagents and, thus, influences the mass transport through the respective layer. Figure 1 shows the effect of the macro-GDM tortuosity on current distribution in the cell under low-humidity operation. In Part I,¹² we described that under low-humidity conditions the local current density initially increases from the cell inlet to the outlet as the dry membrane is hydrated by product water, and then decreases as the membrane becomes fully saturated and oxygen depletion dominates cell performance. It is expected that a higher GDM tortuosity should help membrane hydration, because more water is retained in the membrane rather than being lost to the gas channel. Accordingly, case 1H shows a better performance up to a 60% fractional distance from the cathode inlet, indicating that the current density is mainly controlled by membrane hydration up to this point. The higher GDM tortuosity exacerbates the oxygen transport limitation. Thus, the current density in case 1H starts to drop earlier and shows a lower performance in the downstream region of the cell. In addition, the peak current density in case 1H is also lower due to the higher

* Electrochemical Society Active Member.

^z E-mail: cwx31@psu.edu

Table I. Parametric matrix.

Parameter studied	Baseline	Lower case (case L)	Higher case (case H)
1. Macro-GDM tortuosity	5	2.5	10
2. Micro-GDM tortuosity	5	2.5	10
3. Catalyst layer tortuosity	5	2.5	10
4. Effective ionomer fraction in catalyst layer, $\varepsilon_{mc}^{1.5}$	$0.26^{1.5} = 0.134$	$0.165^{1.5} = 0.067$	$0.416^{1.5} = 0.268$
5. Macro/micro-GDM thermal conductivity, k_{GDM}^{eff} (W/mK)	1.5	0.75	3.0
6. Cathode volumetric exchange current density, $ai_{0,c}^{ref}$ (353 K) (A/m ³)	20000	10000	40000
7. Membrane thickness (μ m)	18	Thicker membrane $0.5 \times \kappa_{mem}^{eff}$ $0.5 \times D_{w,mem}^{eff}$	Thinner membrane $2.0 \times \kappa_{mem}^{eff}$ $2.0 \times D_{w,mem}^{eff}$
8. Contact resistance (m Ω cm ²)	50	0	150
9. Counterflow vs coflow	Coflow		Counterflow

tortuosity and hence lower effective diffusivity of oxygen. The overall performance is higher with the higher GDM tortuosity, showing about 7% improvement in the average current density between the higher and lower bounds. This indicates that water transport is more limiting than oxygen transport under these operating conditions. The average rise in the membrane temperature is similar to the range of current density variations.

The effect of micro-GDM tortuosity is presented in Fig. 2. As expected, the effect is small in the single-phase regime considered in the present model because the micro-GDM is much thinner (60 μ m) than the macro-GDM (175 μ m). However, the micro-GDM is believed to play a more significant role in liquid water transport in a PEFC and its microstructure and wettability have been demonstrated to be important parameters when a two-phase model is employed.¹³ Figure 3 shows a very small effect of the tortuosity in the catalyst layer, which indicates that the gas transport through the catalyst layer plays a negligible role in PEFC performance given that only the single-phase regime is considered here resulting in no flooding within the catalyst layer.

The effect of the catalyst layer ionomer fraction is shown in Fig. 4, where the higher ionomer produces higher performance due to less ionic resistance through the catalyst layer. In this work, notice that the ohmic loss through the two catalyst layers can be even higher than that through the thin membrane (18 μ m). As men-

tioned in Part I, we assume that the proton conductivity of the GORE-SELECT membrane is half of the value of the proton conductivity expressed by Springer et al.,¹ but the full conductivity value is applied to the catalyst layer. Therefore, the ratio of the ohmic resistances through the membrane to that through the two catalyst layers can be estimated as

$$R_{cat} = \frac{2 \times \frac{10 \mu m}{2}}{\kappa_{cat}^{eff}} = \frac{10 \mu m}{(0.26)^{1.5} \kappa_{mem}} \quad [1]$$

$$R_{mem} = \frac{18 \mu m}{\kappa_{mem}^{eff}} = \frac{18 \mu m}{0.5 \kappa_{mem}} \quad [2]$$

$$\frac{R_{mem}}{R_{cat}} = \frac{36 \mu m / \kappa_{mem}}{75.43 \mu m / \kappa_{mem}} = 0.48 \quad [3]$$

This calculation indicates that the ohmic loss through anode and cathode catalyst layers is roughly twice that of the membrane. Therefore, the effect of the catalyst layer ionomer fraction is appreciable, resulting in ~41% difference in the average current density between the lower and higher bounds.

Figure 5 shows the effects of macro/micro-GDM thermal conductivity on current distribution. It is noted in Part I that the thermal

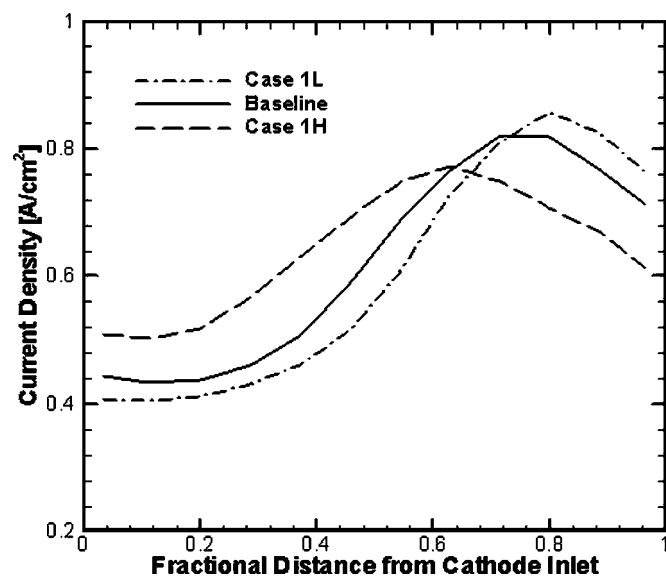


Figure 1. Macro GDM tortuosity effect on current density distributions along the cathode flow. Case 1L: $I_{avg} = 0.603$ A/cm² and $\Delta T_{avg,mem} = 2.05$ K; baseline: $I_{avg} = 0.623$ A/cm² and $\Delta T_{avg,mem} = 2.05$ K; case 1H: $I_{avg} = 0.643$ A/cm² and $\Delta T_{avg,mem} = 2.15$ K.

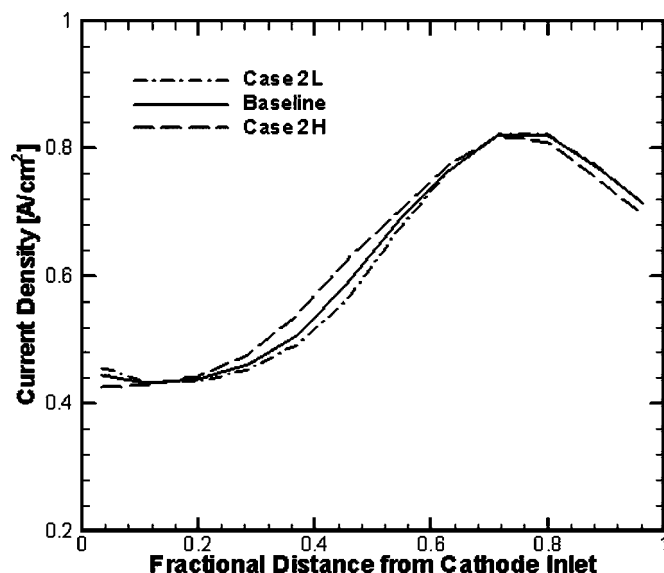


Figure 2. Micro GDM tortuosity effect on current density distributions along the cathode flow. Case 2L: $I_{avg} = 0.618$ A/cm²; baseline: $I_{avg} = 0.623$ A/cm²; and case 2H: $I_{avg} = 0.627$ A/cm².

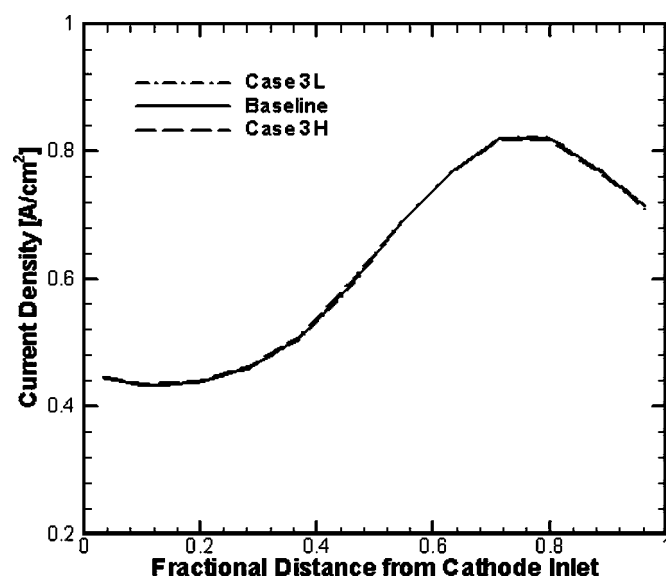


Figure 3. Catalyst layer tortuosity effect on current density distributions along the cathode flow. Case 3L: $I_{\text{avg}} = 0.622 \text{ A/cm}^2$; baseline: $I_{\text{avg}} = 0.623 \text{ A/cm}^2$; and case 3H: $I_{\text{avg}} = 0.623 \text{ A/cm}^2$.

effect in a PEFC strongly depends upon the GDM thermal conductivity, because the primary mechanism of heat removal from the reaction surface is by lateral heat conduction through the GDM in the in-plane direction to the current collecting land. Further, Part I also indicates that the thermal effect is more significant in fuel cell operation at low humidity, because it strongly affects the degree of membrane hydration and, thus, the performance of the PEFC. For these reasons, it is seen in Fig. 5 that the higher GDM thermal conductivity produces higher fuel cell performance due to less membrane temperature rise, which leads to better proton conductivity in the membrane. It is also clearly seen that the peak in current density occurs earlier in the case with higher GDM thermal conductivity, implying that the membrane reaches the fully saturated state faster due to a smaller rise in membrane temperature.

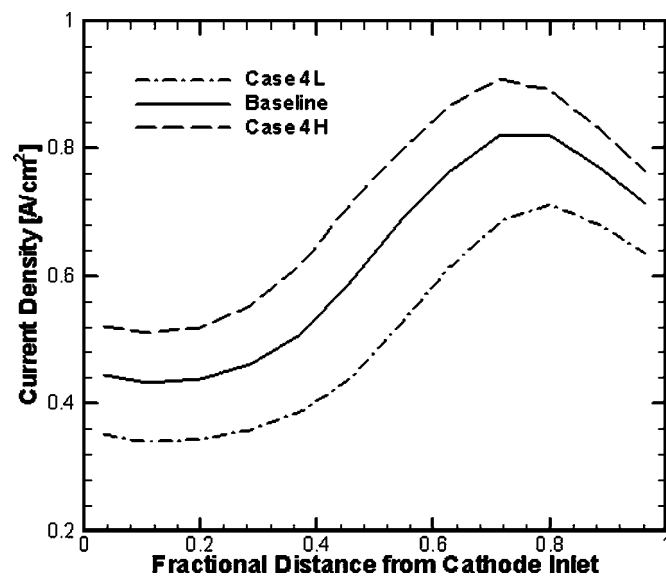


Figure 4. Catalyst layer ionomer fraction effect on current density distributions along the cathode flow. Case 4L: $I_{\text{avg}} = 0.506 \text{ A/cm}^2$; baseline: $I_{\text{avg}} = 0.623 \text{ A/cm}^2$; and case 4H: $I_{\text{avg}} = 0.711 \text{ A/cm}^2$.

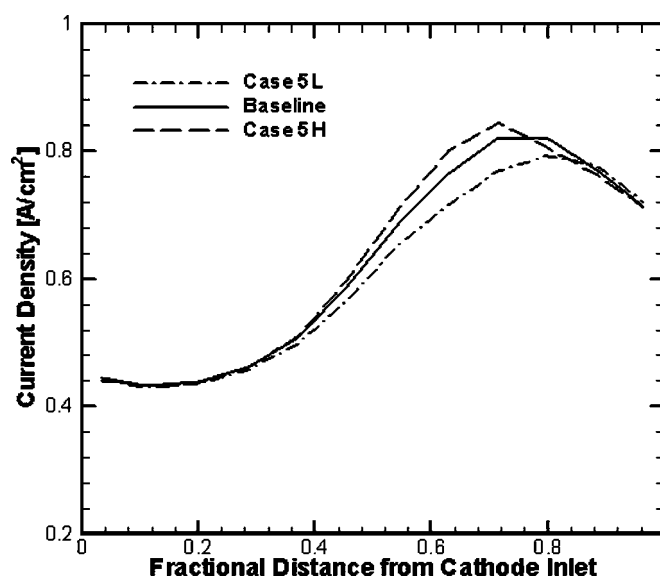


Figure 5. Macro/micro GDM thermal conductivity effect on current density distributions along the cathode flow. Case 5L: $I_{\text{avg}} = 0.606 \text{ A/cm}^2$ and $\Delta T_{\text{avg,mem}} = 3.45 \text{ K}$; baseline: $I_{\text{avg}} = 0.623 \text{ A/cm}^2$ and $\Delta T_{\text{avg,mem}} = 2.05 \text{ K}$; and case 5H: $I_{\text{avg}} = 0.629 \text{ A/cm}^2$ and $\Delta T_{\text{avg,mem}} = 1.15 \text{ K}$.

Figure 6 displays the temperature distribution along the centerline of the membrane in a cross section cutting through the middle of the cell for three different GDM thermal conductivity cases (i.e., case 5L, baseline, and case 5H). A larger overall temperature rise is predicted for the lower GDM thermal conductivity case compared to the high GDM conductivity case. The model also calculates the local temperature difference between adjacent channels and lands of the flow field. The local membrane temperature above a channel is always observed to be greater than that above a land. The magnitude of membrane temperature fluctuations between a channel and a land also strongly depends on the GDM thermal conductivity (see Fig. 6), and a much higher membrane temperature rise in the channel area is predicted with the lower GDM thermal conductivity (i.e., case 5L).

Figure 7 displays the effect of cathode volumetric exchange current density, $ai_{0,c}^{\text{ref}}$, on the current density distribution. This kinetic parameter is the product of the specific catalytically active area and the intrinsic exchange current density of oxygen reduction reaction (ORR). The higher this parameter, the lower the cathode activation loss. With a Tafel slope of 70 mV per decade for ORR, doubling this kinetic parameter amounts to a 21 mV reduction in the cathode activation overpotential. Thus, case 6L and case 6H exhibit 21 mV lower and higher loss compared to the baseline case, respectively. In this range of the $ai_{0,c}^{\text{ref}}$ variation, a roughly 25% difference in the average current density is observed between these higher and lower bounds.

Figure 8 shows the effect of the membrane thickness on current distribution. The effect of the membrane thickness is explored indirectly by adjusting the effective membrane conductivity and water diffusivity rather than changing the actual membrane thickness. The latter would involve remeshing the cell geometry, which is cumbersome in 3D simulations. As expected, the thinner membrane case produces higher performance, because it improves membrane hydration by increasing the rate of back-diffusion, which lowers the ionic resistance. As a result, the thinner membrane case, case 7H, shows about 70% better performance and 1.1 K higher membrane temperature rise on average than the thicker membrane case, case 7L.

In Fig. 9, the effect of contact resistance on current density distribution is presented. The contact resistance defined here includes all interfacial resistances within a PEFC, i.e., at the interface between the catalyst coated membrane (CCM) and GDM and the contact between GDM and current collector lands. A higher contact

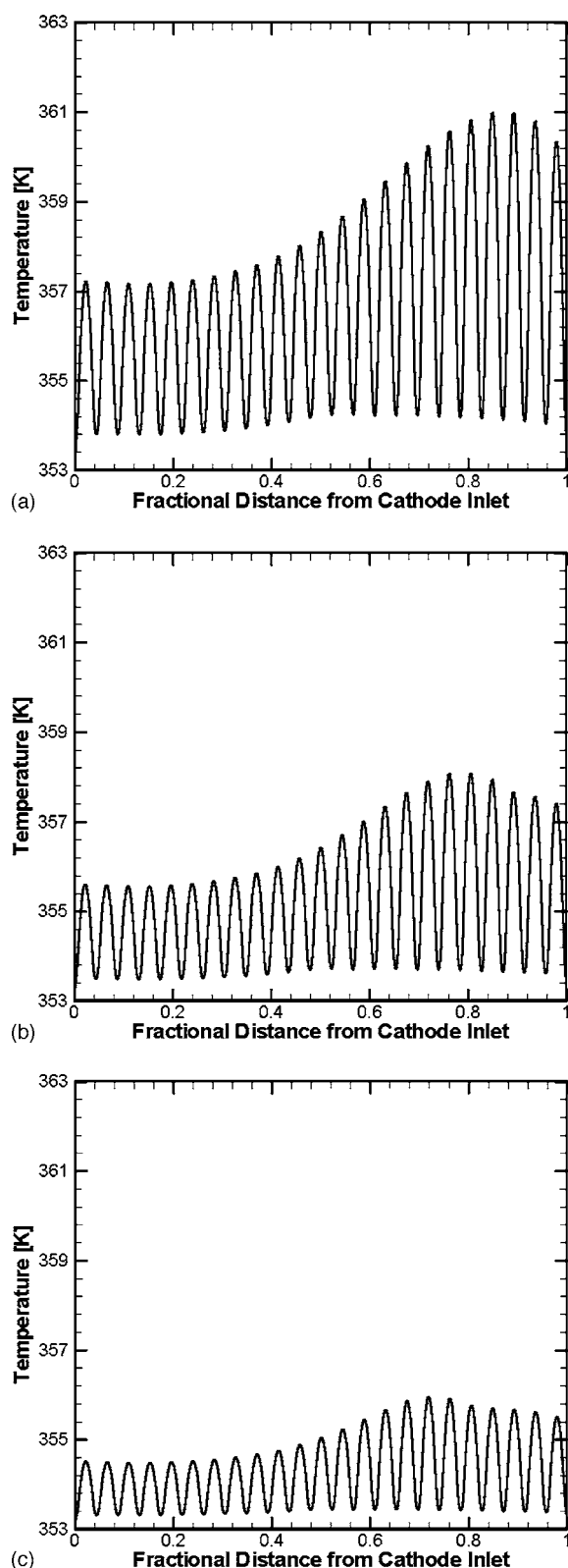


Figure 6. Temperature profiles in the cross section cutting across the middle of fuel cell ($RH_a/RH_c = 75\%/0\%$, $V_{cell} = 0.7$ V).

resistance should result in a lower cell performance but a more uniform current density profile is expected. To evaluate the degree of nonuniformity in current distributions under various contact resistances, the standard deviation (SD) along the fractional distance is calculated by

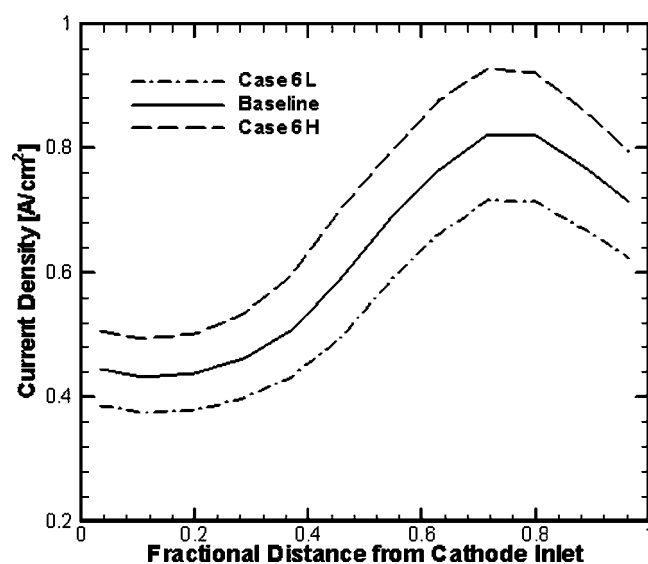


Figure 7. Cathode volumetric exchange current density effect on current density distributions along the cathode flow. Case 6L: $I_{avg} = 0.538$ A/cm²; baseline: $I_{avg} = 0.623$ A/cm²; and case 6H: $I_{avg} = 0.711$ A/cm².

$$SD = \sqrt{\frac{\sum_N (I - I_{avg})^2}{N - 1}} \quad [4]$$

and results are given in the captions of Fig. 9. The uniformity in current distribution increases with contact resistance. Therefore, it can be concluded that if a fuel cell has higher contact resistance, a more uniform current distribution results.

Figure 10 compares the current density profiles in coflow and counterflow of the anode and cathode gas streams. Roughly 15% better performance is predicted in the counterflow case, indicating that overall the membrane is better hydrated in this configuration. However, the effect of counterflow strongly depends on the combination of the anode and cathode inlet RH values. Figure 11 shows the water activity distribution in the cross section cutting through the

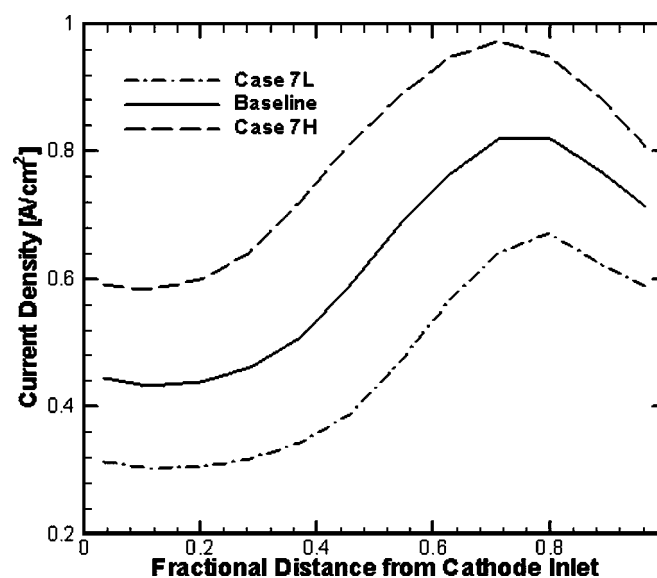


Figure 8. Membrane thickness effect on current density distributions along the cathode flow. Case 7L: $I_{avg} = 0.462$ A/cm² and $\Delta T_{avg,mem} = 1.55$ K; baseline: $I_{avg} = 0.623$ A/cm² and $\Delta T_{avg,mem} = 2.05$ K; and case 7H: $I_{avg} = 0.787$ A/cm² and $\Delta T_{avg,mem} = 2.65$ K.

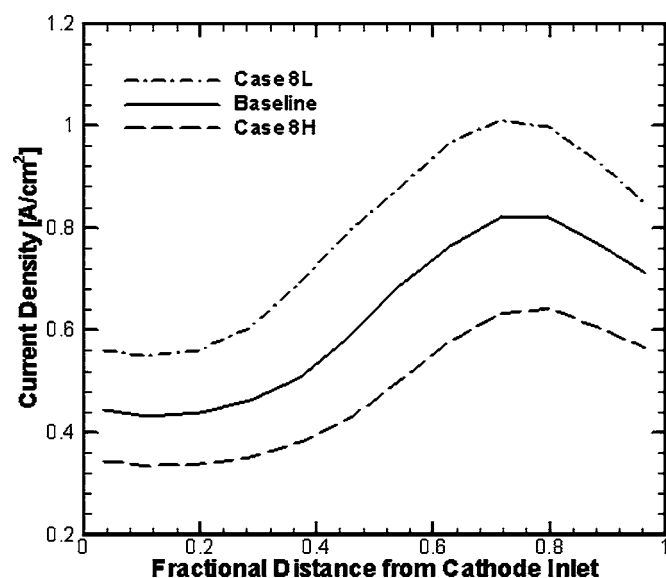


Figure 9. Contact resistance effect on current density distributions along the cathode flow. Case 8L: $I_{\text{avg}} = 0.786 \text{ A/cm}^2$ and $\text{SD} = 0.1802$; baseline: $I_{\text{avg}} = 0.623 \text{ A/cm}^2$ and $\text{SD} = 0.1577$; and case 7H: $I_{\text{avg}} = 0.476 \text{ A/cm}^2$ and $\text{SD} = 0.1246$.

middle of the cell for the coflow and counterflow cases, where it is seen that the membrane water activity of the counterflow case is higher than that in coflow, clearly indicating that more efficient membrane hydration is achieved in counterflow.

Conclusions

Using a representative low-humidity condition ($T = 80^\circ\text{C}$, $\text{RH}_a/\text{RH}_c = 75\%/0\%$) and 0.7 V operation, a parametric study has been performed for eight important design and operating parameters. The main focus of this study has been to develop a quantitative understanding of PEFCs operated under low-humidity conditions in which the cell performance is governed by both membrane hydration and oxygen transport. The following specific conclusions can be drawn.

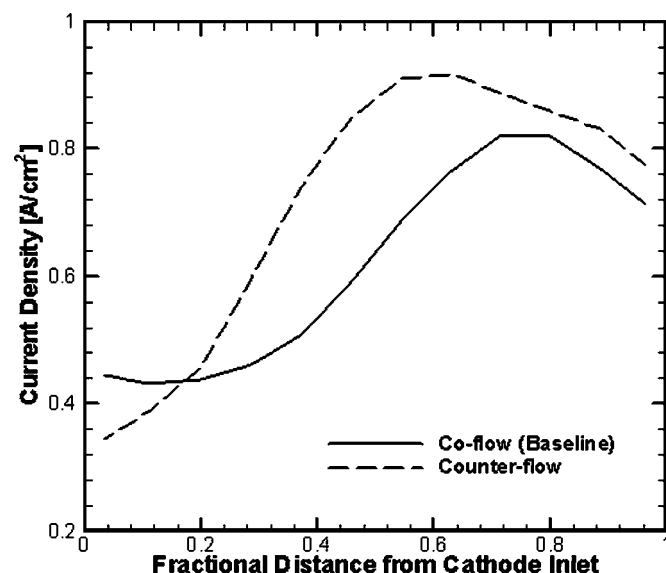


Figure 10. Comparison between current density distributions in coflow and counterflow. Coflow (baseline): $I_{\text{avg}} = 0.623 \text{ A/cm}^2$, and counterflow: $I_{\text{avg}} = 0.712 \text{ A/cm}^2$.

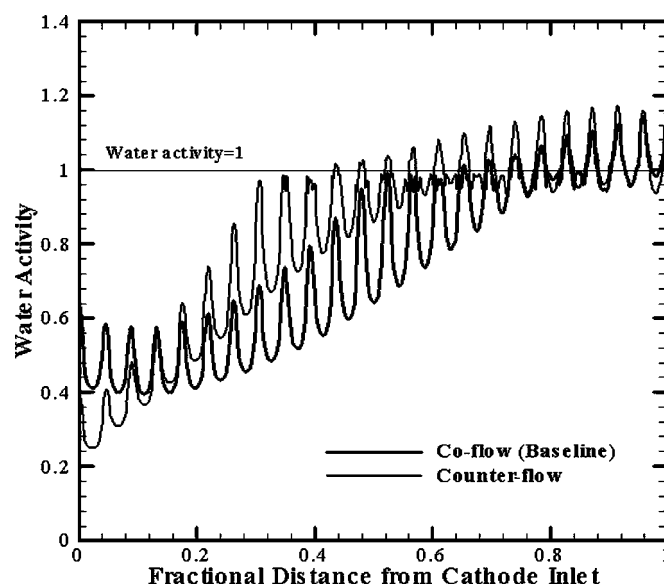


Figure 11. Coflow and counterflow water activity profiles in the cross section cutting across the middle of the fuel cell.

As expected, the model finds that the catalyst layer ionomer fraction (case 4), ORR kinetic parameter (case 6), membrane thickness (case 7), and contact resistance (case 8) considerably influence the overall PEFC performance.

Unexpectedly, the macro-GDM tortuosity (case 1), GDM thermal conductivity (case 5), and counterflow configuration (Fig. 10 and 11) are found to be significant design parameters. They strongly affect the degree of membrane hydration, and hence influence the current density distribution as well as the overall cell performance.

The tortuosity effect of the micro-GDM (case 2) and catalyst layer (case 3) is found to be small in the single-phase regime of interest here.

In summary, the numerical model has been shown to be a powerful tool not only for understanding the complex and interacting phenomena in PEFCs, but also in the search for optimal water and thermal management strategies.

Acknowledgments

Financial support of this research by W. L. Gore & Associates, Inc. is gratefully acknowledged.

The Pennsylvania State University assisted in meeting the publication costs of this article.

List of Symbols

- a water activity or effective catalyst area per unit volume (m^2/m^2)
- D mass diffusivity of species (m^2/s)
- i_0 exchange current density (A/m^2)
- I current density (A/m^2)
- j transfer current (A/m^3)
- R ionic resistance ($\Omega \text{ m}^2$)
- RH relative humidity
- SD standard deviation
- T temperature (K)

Greek

- ϵ volume fraction of gaseous phase in porous region
- ϵ_{mc} volume fraction of ionomer phase in catalyst layer
- κ ionic conductivity (S/m)
- τ tortuosity in porous region or viscous stress (N/m^2)

Superscripts

- eff effective value in porous region
- ref reference value

Subscripts

a	anode
avg	average value
c	cathode
cat	catalyst
GDM	gas diffusion media
mem	membrane
w	water
0	standard condition, 298.15 K, and 101.3 kPa (1 atm)

References

1. T. E. Springer, T. A. Zawodinski, and S. Gottesfeld, *J. Electrochem. Soc.*, **136**, 2334 (1991).
2. T. E. Springer, M. S. Wilson, and S. Gottesfeld, *J. Electrochem. Soc.*, **140**, 3513 (1993).
3. V. Gurau, H. Liu, and S. Kakac, *AIChE J.*, **44**, 2410 (1998).
4. T. Okada, G. Xie, and M. Meeg, *Electrochim. Acta*, **97**, 2141 (1998).
5. T. V. Nguyen and R. E. White, *J. Electrochem. Soc.*, **140**, 2178 (1993).
6. J. S. Yi and T. V. Nguyen, *J. Electrochem. Soc.*, **145**, 1149 (1998).
7. A. Rowe and X. Li, *J. Power Sources*, **102**, 82 (2001).
8. N. Djilali and D. Lu, *Int. J. Therm. Sci.*, **41**, 29 (2002).
9. M. Wöhr, K. Bolwin, W. Schnumberger, M. Fischer, and W. Neubrand, *Int. J. Hydrogen Energy*, **23**, 213 (1998).
10. D. P. Wilkinson and J. St-Pierre, *J. Power Sources*, **113**, 101 (2003).
11. T. Berning and N. Djilali, *J. Power Sources*, **124**, 440 (2003).
12. H. Ju, C. Y. Wang, S. Cleghorn, and U. Beuscher, *J. Electrochem. Soc.*, **152**, A1645 (2005).
13. U. Pasaogullari and C. Y. Wang, *Electrochim. Acta*, **49**, 4359 (2004).